Inorg. Chem. **1996,** *35,* 6987−6994 **6987**

New Zr$_6$MTe$_2$ (M = Mn, Fe, Co, Ni, Ru, Pt), Zr$_6$Fe$_{0.6}$Se$_{2.4}$, and Zr$_6$Fe$_{0.57}$S$_{2.43}$ Intermetallics: Structural Links between Binary (Zr,Hf)$_3$M Alloys and Porous Metal-Rich Tellurides

Chwanchin Wang and Timothy Hughbanks*

Department of Chemistry, Texas A&M University, College Station, Texas 77843-3255

Received May 23, 1996[⊗]

The synthesis of the group IV ternary chalcogenides Zr$_6$MTe$_2$ (M = Mn, Fe, Co, Ni, Ru, Pt) and Zr$_6$Fe$_{1-x}$Q$_{2+x}$ (Q = S, Se) is reported, as are the single-crystal structures of Zr$_6$FeTe$_2$, Zr$_6$Fe$_{0.6}$Se$_{2.4}$, and Zr$_6$Fe$_{0.57}$S$_{2.43}$. The structure of Zr$_6$FeTe$_2$ was refined in the hexagonal space group $P\bar{6}2m$ (No. 189, $Z = 1$) with lattice parameters $a = 7.7515(5)$ Å and $c = 3.6262(6)$ Å, and the structures of Zr$_6$Fe$_{0.6}$Se$_{2.4}$ and Zr$_6$Fe$_{0.57}$S$_{2.43}$ were refined in the orthorhombic space group *Pnnm* (No. 58, $Z = 4$) with lattice parameters $a = 12.737(2)$ Å, $b = 15.780(2)$ Å, and $c = 3.5809(6)$ Å and $a = 12.519(4)$ Å, $b = 15.436(2)$ Å, and $c = 3.4966(6)$ Å, respectively. The cell parameters of Mn-, Co-, Ni-, Ru-, and Pt-containing tellurides were also determined. The Zr$_6$ZTe$_2$ compounds are isostructural with Zr$_6$CoAl$_2$, while Zr$_6$Fe$_{1-x}$Q$_{2+x}$ (Q = S, Se) were found to adopt a variant of the Ta$_2$P-type structure. Chains of condensed M-centered, tetrakaidecahedra of zirconium constitute the basic structural unit in all these compounds. The modes of cross-linking that give rise to the Zr$_6$FeTe$_2$ and Zr$_6$Fe$_{1-x}$Q$_{2+x}$ structures, differences among the title compounds, and the influence of chalcogen size differences are discussed. The stoichiometric nature of Zr$_6$FeTe$_2$ and its contrast with sulfur and selenium congeners apparently result from a Te−Fe size mismatch. The importance of stabilization of both Zr$_6$FeSe$_2$ and Zr$_6$FeTe$_2$ compounds by polar intermetallic Zr−Fe bonding is underscored by a bonding analysis derived from electronic band structure calculations.

Introduction

Considerable recent research has focused on the exploration of reduced ternary group IV and V chalcogenides with novel metal−metal-bonded frameworks. This has led to the discovery of many new compounds, such as MM′Te$_2$, (M = Nb, Ta; M′ = Fe, Co, Ni),[1−6] Ta$_{1.09}$Fe$_{2.39}$Te$_4$,[7] Ta$_2$M$_3$Q$_5$ (M = Ni, Pd; Q = Se, Te),[4,8,9] TaCo$_2$Te$_2$,[10] TaFe$_{1.25}$Te$_3$,[11] TaNi$_{2.05}$Te$_3$,[12] NbNi$_{2.38}$Te$_3$,[13] MM′$_3$Te$_4$ (M = Na, K, Rb, Cs; M′ = Zr, Hf),[14] Zr$_4$As$_3$Te$_5$,[15] MXQ phases (M = Zr, Hf; X = Si, Ge, As, Sb; Q = S, Se, Te),[16−19] and some isostructural quasi-ternary zirconium tellurides.[20] A structural motif that has emerged in the chemistry of more metal-rich compounds is the M-centered tricapped trigonal prism (M-centered tetrakaidecahedron) shown in **1**. In this structural building block, late transition metals (M) are surrounded by nine early metals (Nb, Ta, Hf) that serve as vertices of the surrounding tetrakaidecahedron. Such tricapped trigonal prisms are observed in the structures of Ta$_9$M$_2$S$_6$ (M = Fe, Co, Ni),[21,22] Ta$_{11}$M$_2$Se$_8$ (M = Fe, Co, Ni),[23] Ta$_8$MSe$_8$ (M = Co, Ni),[24] Nb$_6$MS$_2$ (M = Fe, Co, Ni),[25] Nb$_8$Ni$_2$S$_4$,[26] Nb$_9$Ni$_{2-x}$S$_{3+x}$,[25] Hf$_8$MTe$_6$ (M = Fe, Co, Ni),[27] and Hf$_5$MTe$_3$ (M = Fe, Co, Ni).[28] Similarly, chains of condensed, M-centered square antiprisms are found in Ta$_4$MTe$_4$ and Nb$_4$MTe$_4$ (M = Al, Si, Cr−Ni).[29,30] No ternary zirconium chalcogenides have been reported that possess similar metal−metal-bonded frameworks.

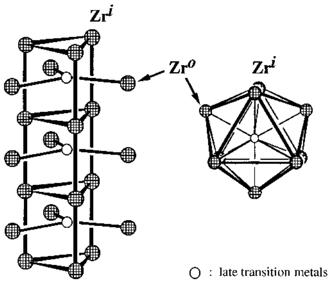

1

Examination of structures and bonding in these novel metal−metal-bonded compounds implicates the strong bonding between

---

[⊗] Abstract published in *Advance ACS Abstracts*, November 1, 1996.

(1) Li, J.; Badding, M. E.; DiSalvo, F. J. *Inorg. Chem.* **1992**, *31*, 1050.
(2) Huang, B.; Shang, M.; Huang, J. *Jiegou Huaxue* **1989**, *8*, 145.
(3) Huang, B.; Shang, M.; Huang, J. *Jiegou Huaxue* **1988**, *1*, 133.
(4) Tremel, W. *Angew. Chem., Int. Ed. Engl.* **1991**, *30*, 840.
(5) Tremel, W. *J. Chem. Soc., Chem. Commun.* **1991**, 1405.
(6) Neuhausen, J.; Stork, K.-L.; Potthoff, E.; Tremel, W. *Z. Naturforsch.* **1992**, *47b*, 1203.
(7) Neuhausen, J.; Tremel, W. *J. Alloys Compd.* **1994**, *204*, 215.
(8) Tremel, W. *Angew. Chem., Int. Ed. Engl.* **1993**, *32*, 1752.
(9) Neuhausen, J.; Tremel, W. *Proceedings: Soft Chemistry Routes to the New Materials*; Trans Tech Publications: Aedermannsdorf, Switzerland, 1994.
(10) Tremel, W. *Angew. Chem., Int. Ed. Eng.* **1992**, *31*, 217.
(11) Badding, M. E.; Li, J.; Disalvo, F. J.; Zhou, W.; Edwards, P. P. *J. Solid State Chem.* **1992**, *100*, 313.
(12) Neuhausen, J.; Evstafyev, V. K.; Kremer, R. K.; Tremel, W. *Chem. Ber.* **1994**, *127*, 1621.
(13) Neuhausen, J.; Finckh, E. W.; Tremel, W. *Inorg. Chem.* **1995**, *34*, 3823.
(14) Wang, C. C.; Abdon, R. L.; Hughbanks, T.; Reibenspies, J. *J. Alloys Compd.* **1995**, *226*, 10.
(15) Mosset, A.; Jeannin, Y. *J. Less-Common Met.* **1972**, *26*, 285.
(16) Haneveld, A. J. K.; Jellinek, F. *Recl. Trav. Chim. Pays-Bas* **1964**, *83*, 776.
(17) Onken, H.; Vierheilig, K.; Hahn, H. *Z. Anorg. Allg. Chem.* **1964**, *233*, 267.
(18) Barthelat, J.-C.; Jeannin, Y.; Rancurel, J.-F. *C. R. Acad. Sci. Ser. II: Mec., Phys., Chim., Astron.* **1969**, *268*, 1756.
(19) Barthelat, J. C.; Jeannin, Y. *J. Less-Common Met.* **1972**, *26*, 273.
(20) Wang, C.; Hughbanks, T. *Inorg. Chem.* **1995**, *34*, 5224.
(21) Harbrecht, B.; Franzen, H. F. *J. Less-Common Met.* **1985**, *113*, 349.
(22) Harbrecht, B. *J. Less-Common Met.* **1986**, *124*, 125.
(23) Harbrecht, B. *J. Less-Common Met.* **1988**, *141*, 59.
(24) Conrad, M.; Harbrecht, B. *J. Alloys Compd.* **1993**, *197*, 57.
(25) Harbrecht, B. *Z. Kristallog.* **1988**, *182*, 118.
(26) Harbrecht, B. Habiltation Thesis, Unversität Dortmund, 1989.
(27) Abdon, R. L.; Hughbanks, T. *Chem. Mater.* **1994**, *6*, 424.
(28) Abdon, R. L.; Hughbanks, T. *J. Am. Chem. Soc.* **1995**, *117*, 10035.
(29) Badding, M. E.; DiSalvo, F. J. *Inorg. Chem.* **1990**, *29*, 3952.
(30) Neuhausen, J.; Finckh, E. W.; Tremel, W. *Chem. Ber.* **1995**, *128*, P569.

S0020-1669(96)00610-6 CCC: $12.00

early and late transition metals as the key factor stabilizing these compounds. This conclusion is in accord with the Lewis acid-base-bonding model offered by Brewer and Wengert to rationalize the large (negative) heats of formation of binary early−late transition alloys.[31] This model posits that donor d electrons of late transition metals are donated to empty acceptor orbitals of early transition metals and that the most negative heats of formation were expected for alloys in which the interactions are optimized. While these ideas have found considerable currency among investigators with an exclusive interest in intermetallics, they have not been used by the broader community of inorganic chemists (or even by solid state chemists) as a synthetic guide. We have sought both to explore the range of compounds for which early−late intermetallic bonding is important and to gain insight as to *why* it is important by studying new compounds' electronic structures.[27,28] A fuller discussion of the motivations for this work is given in recent publications.[28,32]

Brewer et al. predicted that the binary alloys with the largest heats of formation would be those involving Zr and Hf with group X transition metals. For recent experimental data in support of this hypothesis, see a study by Topor and Kleppa.[33] The thermodynamic trends exhibited by the binary early−late alloys of Nb, Ta, Zr, and Hf suggested that while the driving force for Zr−M bond formation is not as great as for Hf−M bonds, it should generally be larger than that for Nb−M or Ta−M bonds. This expectation, taken together with Harbrecht's synthesis of the niobium and tantalum compounds cited above, led us to explore the Zr-rich chemistry of ternary zirconium chalcogenides.

In this paper we report the synthesis and structures of Zr_6MTe_2 (M = Mn, Fe, Co, Ni, Ru, Pt), $Zr_6Fe_{0.6}Se_{2.4}$, and $Zr_6Fe_{0.57}S_{2.43}$ compounds. These are the first ternary zirconium chalcogenides to exhibit metal-centered tricapped trigonal prismatic clusters as a basic structural unit. The structural relationships between the title compounds and other related compounds will be discussed and may help to shed light on the exploration of the early transition metal-rich chalcogenide systems. The results from electronic band structures serve to aid the analysis of the structural features and electronic properties.

Experimental Section

Syntheses. All operations prior to reaction were carried out in a glovebox under a N_2 atmosphere. Elemental starting materials were Zr (99.2%, including 4.5 wt % Hf, Johnson Matthey), Te (99.997%, Aldrich), Se (99.99%, Johnson Matthey), S (99.99%, Fisher), Mn (99.9%, Johnson Matthey), Fe (99.99%, Aldrich), Co (99.998%, Johnson Matthey), Ni (99.996%, Johnson Matthey), Ru (99.997%, Johnson Matthey), and Pt (99.997%, Johnson Matthey). Elemental mixtures were pressed into pellets and sealed in Nb capsules, which were in turn sealed in evacuated (~10^{-4} Torr) silica tubes. Zr_6MTe_2 (M = Mn, Fe, Co, Ni) compounds were first obtained as a major product with a loaded composition of Zr_3MTe and identified as adopting a common structure type by powder diffraction analysis. Several subsequent reactions were carried out (at 1000 °C for 3 weeks) in the Zr−Fe−Te system, and the results suggested that the new compounds had a more Zr-rich composition. After a period of such experimentation, the correct composition emerged. A 0.5 g mixture of Zr, Fe, and Te at a ratio of 6:1:2 was finely ground and sealed in a Nb capsule that was in turn sealed in an evacuated silica tube. To reduce ultimate Te volatilization via prereduction, the reaction vessel was heated to 550 °C over 6 h and maintained at that temperature for 2 days. The temperature was then uniformly raised to 850 °C over 12 h and held at 850 °C for 3 days. The reaction vessel was cooled radiatively to room temperature. The resulting powder was cold-pressed into a pellet and melted (~50 A, 32 V) three times for 1 min on an oxygen-free copper hearth under an argon atmosphere. A 0.4% mass loss due to Te volatilization during the melting process was determined by difference. This reaction yielded only Zr_6FeTe_2. Single crystals of Zr_6FeTe_2 were obtained by the same procedure in a reaction loaded with Zr:Fe:Te = 4:1:1.

Table 1. Lattice Parameters (Å) and Cell Volumes (Å^3) of Ternary Group IV Compounds[a]

M	*a*	*c*	volume
	Zr_6MTe_2		
Mn	7.7505(7)	3.6570(9)	190.25(6)
Fe	7.7515(5)	3.6262(6)	188.69(4)
Co	7.7244(7)	3.6432(6)	188.26(5)
Ni	7.6764(6)	3.6958(9)	188.60(6)
Ru	7.8200(7)	3.6299(7)	192.24(5)
Pt	7.7144(8)	3.7310(8)	192.29(6)
	Hf_6MTe_2		
Fe	7.6533(9)	3.5656(8)	180.87(6)
Co	7.6468(7)	3.5590(8)	180.23(6)

[a] Refined from Guinier powder diffraction patterns using Si as an internal standard.

All Zr_6MTe_2 (M = Mn, Fe, Co, Ni, Ru, Pt) compounds could be synthesized both from arc-melting reactions in the manner described above for Zr_6FeTe_2 and, as powders, by forgoing the arc-melting step. In each of the arc-melting reactions, the weight loss determined by difference was less than 3%. Sealed-tube reactions were carried out as described above: elemental mixtures were sealed in Nb capsules, which were in turn sealed in evacuated silica tubes and then subjected to a temperature profile similar to that described above. However, in the final heating step, the temperature was raised to 950 °C over 24 h and held at 950 °C for 14 days. The reaction vessels were cooled to 350 °C over 2 days, and then the reaction was quenched to room temperature. The desired product in each Zr_6MTe_2 (M = Mn, Fe, Co, Ni) reaction was obtained in high yields (>80%); the only observed byproduct was Zr_5Te_4. Synthesis of the Ru- and Pt-containing congeners yielded mostly Zr_5Te_4 and no more than a 30% yield of the intended ternary compounds.

Zr_6FeQ_2 (Q = S, Se) can be synthesized directly by mixing elements in stoichiometric proportions and conducting the arc-melting reactions in the manner described in the preparation of Zr_6FeTe_2. However, microprobe analysis on selected crystals from the products of both Zr_6FeSe_2 and Zr_6FeS_2 reactions showed them to be nonstoichiometric with the approximate compositions $Zr_6Fe_{0.57(1)}Se_{2.40(1)}$ and $Zr_6Fe_{0.56(2)}S_{2.44(2)}$, respectively. No other elements heavier than Na, including Nb, were found in either case.

X-ray Crystallography. A chunk crystal of Zr_6FeTe_2 having approximate dimensions 0.20 × 0.11 × 0.08 mm was mounted in a glass capillary. X-ray data were collected on a Siemens R3m/V diffractometer with graphite-monochromated Mo Kα radiation at room temperature. Cell constants and an orientation matrix were obtained from a least squares refinement using the setting angles from six centered reflections. This cell was refined by centering on 26 reflections in the range $15° < 2\theta < 30°$. Cell parameters in Table 1 are refined from Guinier powder diffraction patterns. Intensity data were collected by $\theta-2\theta$ scans for reflections with $2\theta < 50°$. Three check reflections monitored throughout the data collection process showed no significant trends. A hemisphere of the data was collected ($+h$, $\pm k$, $\pm l$) to gain the advantage of averaging. The data were corrected for absorption using the ψ-scan technique, based on three reflections. Since it is isostructural with Zr_6CoAl_2,[34] the coordinates of Zr, Co, and Al were respectively used to refine the coordinates of Zr, Fe, and Te in Zr_6FeTe_2. The structure refinement was based on F^2 using the SHELX-93 program.[35] Isotropic refinement of the structure was uneventful and yielded atoms with reasonable thermal parameters with a residual of 2.42%. Anisotropic refinement of Zr_6FeTe_2 again showed reasonable

---

(31) Brewer, L.; Wengart, P. R. *Metall. Trans.* **1973**, *4*, 2674.

(32) Hughbanks, T. *J. Alloys Compd.* **1995**, *229*, 40.

(33) Topor, L.; Kleppa, O. J. *J. Less-Common Met.* **1989**, *155*, 61.

(34) Kryiyakevich, P. I.; Burnashova, V. V.; Markiv, V. Y. *Dopov. Akad. Nauk. Ukr. RSR, Ser. A: Fiz-Tekhn. Mat. Nauki* **1970**, *32*, 828.

(35) Sheldrick, G. M. In *SHELXTL-93 User Guide*, version 3.4; Sheldrick, G. M., Ed.; Nicolet Analytical X-ray Instruments: Göttingen, Germany, 1993.

Table 2. Crystallographic Data for Zr_6FeTe_2, $Zr_6Fe_{0.6}Se_{2.4}$, and $Zr_6Fe_{0.57}S_{2.43}$

chemical formula	Zr_6FeTe_2	$Zr_6Fe_{0.6}Se_{2.4}$	$Zr_6Fe_{0.57}S_{2.43}$
a, Å	7.7517(5)	12.737(2)	12.519(4)
b, Å		15.780(2)	15.436(2)
c, Å	3.6262(6)	3.5809(6)	3.4966(6)
V, Å^3	188.69(4)	719.7(2)	675.8(3)
Z	1	4	4
fw	858.37	770.33	657.18
space group	$P\bar{6}2m$ (No. 189)	*Pnnm* (No. 58)	*Pnnm* (No. 58)
T, °C	20	20	20
λ, Å	0.710 73	0.710 73	0.710 73
ρ_{calcd}, g/cm^3	7.553	7.109	6.459
μ, mm^{-1}	17.291 mm^{-1}	21.551 mm^{-1}	10.724 mm^{-1}
R^a	2.18	3.77	5.23
$R_w{}^b$	5.65	7.16	10.39

[a] $R(F) = \sum(|F_o| - |F_c|)/\sum(|F_o|)$. [b] $R_w(F^2) = \{\sum[w(F_o{}^2 - F_c{}^2)^2]/\sum[w(F_o{}^2)^2]\}^{1/2}$, $w = 1/[\sigma^2(F_o{}^2) + (xP)^2 + yP]$ where $P = (\max(F_o{}^2,0) + 2F_c{}^2)/3$.

thermal parameters and gave the final residual $R = 2.18\%$. The largest remaining peak in the final Fourier difference map was 0.565 e$^-$/Å^3 located near Te1 in the framework of the structure.

Needle crystals of both $Zr_6Fe_{0.6}Se_{2.4}$ and $Zr_6Fe_{0.57}S_{2.43}$ having approximate dimensions 0.18 × 0.06 × 0.04 mm and 0.40 × 0.02 × 0.02 mm, respectively, were mounted in glass capillaries. Both X-ray data sets were collected on an upgraded Siemens P4 diffractometer with graphite-monochromated Mo Kα radiation at room temperature. Cell constants and an orientation matrix were obtained from a least squares refinement using the setting angles from 11 and 10 centered reflections in the range $15° < 2\theta < 33°$, respectively. Cell parameters in Table 2 were refined from Guinier powder diffraction patterns. Intensity data were collected by $\theta-2\theta$ scans for reflections with $2\theta < 50°$ for $Zr_6Fe_{0.6}Se_{2.4}$ and $2\theta < 60°$ for $Zr_6Fe_{0.57}S_{2.43}$. Three check reflections monitored throughout the data collection process showed no significant trends. To gain the advantage of averaging, a full sphere and a hemisphere ($+h$, $\pm k$, $\pm l$) of data were respectively collected for $Zr_6Fe_{0.6}Se_{2.4}$ and $Zr_6Fe_{0.57}S_{2.43}$. The data were corrected for absorption using the ψ-scan technique, based on three reflections. Since both compounds are isostructural with Nb_6FeSe_2,[25,26] that compound served as a starting model for $Zr_6Fe_{0.6}Se_{2.4}$ and $Zr_6Fe_{0.6}S_{2.4}$. The structure refinement was based on F^2 using the SHELX-93 program. Isotropic refinement of the $Zr_6Fe_{0.6}Se_{2.4}$ structure using a stoichiometric Zr_6FeSe_2 model showed that the thermal coefficient of the Fe atom was 50% smaller than those of Se atoms with a residual (*R*) of 5.36%. Partial Se occupancy of the Fe site was introduced subject to the constraints that the summed Se and Fe occupancies were unity (i.e., the composition was $Zr_6(Fe_{1-x}Se_x)Se_2$) and that these atoms' thermal parameters were constrained to be equal. This yielded a residual of 5.14% and a selenium occupancy of 40% with reasonable thermal coefficients for the Fe (Se) atoms and in very good agreement with the microprobe data. Anisotropic refinement of $Zr_6Fe_{0.6}Se_{2.4}$ showed the thermal ellipsoids of all atoms to be fairly isotropic and gave the final residual $R = 3.77\%$. The largest remaining peak in the final Fourier difference map was 4.34 e$^-$/Å^3 located near Zr5 in the framework of the structure. Isotropic refinement of the $Zr_6Fe_{0.57}S_{2.43}$ structure showed that the thermal coefficient of the Fe atom was two times larger than those of S atoms with a residual of 8.13%. Partial S occupancy of the Fe site was introduced as was the refinement in $Zr_6Fe_{0.57}Se_{2.43}$. A sulfur occupancy of 43% was obtained and converged to a residual of 7.90%. Again, the refined occupancy is in very good agreement with microprobe data. Anisotropic refinement of the atomic parameters resulted in pancake-like thermal ellipsoids along the *bc* plane. After program DIFABS was used to correct for absorption,[36] anisotropic refinement of $Zr_6Fe_{0.57}S_{2.43}$ showed the thermal ellipsoids of all atoms to be fairly isotropic and gave the final residual $R = 5.23\%$. Two negative reflections were suppressed during the refinement. The largest remaining peak in the final Fourier difference map was 3.42 e$^-$/Å^3 located near Zr5 in the framework of the structure. A summary of crystal and data collection parameters for all structures is listed in Table 2, and final atomic coordinates are located in Table 3.

Table 3. Atomic Coordinates and Equivalent Isotropic Displacement Parameters

	x	*y*	*z*	$U_{eq}{}^a$ (Å^2 × 10^3)
		Zr_6FeTe_2		
Zr1	0.5961(2)	0.0	0.0	7(1)
Zr2	0.2428(2)	0.0	0.5	7(1)
Te1	0.3333	0.6667	0.5	6(1)
Fe1	0.0	0.0	0.0	10(1)
		$Zr_6Fe_{0.6}Se_{2.4}$		
Zr1	0.1187(1)	0.0796(1)	0.0	8(1)
Zr2	0.1970(1)	0.2982(1)	0.0	8(1)
Zr3	0.4734(1)	0.8957(1)	0.0	11(1)
Zr4	0.0856(1)	0.7547(1)	0.0	7(1)
Zr5	0.1634(2)	0.5180(1)	0.0	14(1)
Zr6	0.4131(1)	0.4214(1)	0.0	10(1)
Se1	0.3134(1)	0.1518(1)	0.0	8(1)
Se2	0.4291(1)	0.7097(1)	0.0	8(1)
Fe1/Se3	0.2435(2)	0.9143(1)	0.0	12(1)
		$Zr_6Fe_{0.57}S_{2.43}$		
Zr1	0.1206(1)	0.0851(1)	0.0	10(1)
Zr2	0.1959(1)	0.2941(1)	0.0	9(1)
Zr3	0.4732(1)	0.8947(1)	0.0	12(1)
Zr4	0.0840(1)	0.7508(1)	0.0	9(1)
Zr5	0.1656(1)	0.5213(1)	0.0	12(1)
Zr6	0.4119(1)	0.4208(3)	0.0	10(1)
S1	0.3143(3)	0.1521(3)	0.0	10(1)
S2	0.4326(3)	0.7116(2)	0.0	10(1)
Fe1/S3	0.2433(2)	0.9123(2)	0.0	14(1)

[a] Equivalent isotropic *U* defined as one-third of the trace of the orthogonalized $\mathbf{U}_{ij}$ tensor.

Results and Discussion

Synthetic Aspects. Investigation of the thermal stability of Zr_6FeQ_2 (Q = S, Se) and Zr_6MTe_2 (M = Mn, Fe, Co, Ni, Ru, Pt) compounds shows that they exist over a wide temperature range. Attempts to obtain good synthetic yields of all the ternary tellurides via sealed-tube reactions (1000 °C for 14 days) were thwarted by the formation of the binary Zr_5Te_4.[37] This binary side product persisted even in reactions heated for extended time periods. We therefore resorted to arc-melting reactions to insure that kinetic barriers in the synthesis were overcome; for compounds containing first-row transition metals (M = Mn, Fe, Co, Ni), yields of the ternaries improved markedly. In every instance, the ternary compounds so obtained remained stable when subsequently annealed at 1000 °C for 7 days. Isostructural Hf_6MTe_2 (M = Fe, Co) compounds could also be synthesized by the methods described in the synthesis of Zr_6MTe_2 compounds, and their cell parameters are listed in Table 1. Attempts to synthesize isostructural Nb_6FeTe_2 and Hf_6MQ_2 (M = Fe, Co; Q = S, Se) compounds were unsuccessful; however, powder patterns for products obtained in these attempts contain lines for phases that are, as yet, unidentified.

Yields of both Ru- and Pt-centered tellurides, Zr_6MTe_2, remained rather poor even when an arc-melting step was included. The reasons for this are not understood since powder diffraction data indicate the presence of only Zr_6MTe_2 (M = Ru, Pt) and Zr_5Te_4 in the products, and we were therefore unable to identify the fate of Ru (Pt) that is not incorporated into the Zr_6MTe_2 phase. It is possible that these larger interstitials substitute for Te so that the Zr_6MTe_2 phases are in fact nonstoichiometric phases that should be formulated as $Zr_6M(Te_{2-x}M_x)$. This possible nonstoichiometry is currently under investigation; we will discuss structural correlations and nonstoichiometry further below.

Structure of Zr_6FeTe_2. The compounds Zr_6MTe_2 (M = Mn, Fe, Co, Ni, Ru, Pt) are new members with the Zr_6CoAl_2 structure

---

(36) Walker, N.; Stuart, D. *Acta Crystallogr.* **1983**, *A39*, 158.

(37) Brattås, L.; Kjekshus, A. *Acta Chem. Scand.* **1971**, *25*, 2350.

Table 4. Important Interatomic Distances (Å) for Zr_6FeTe_2[a]

Zr^{i}−Zr^{i}		Fe−Zr^{i}	
Zr2−Zr2 (2×)	3.260(3)	Fe−Zr2 (6×)	2.613(1)
Zr2−Zr2 (2×)	3.626(1)		
		Fe−Zr^{o}	
Zr^{i}−Zr^{o}		Fe−Zr1 (3×)	3.131(2)
Zr2−Zr1 (4×)	3.277(1)		
		Fe−Fe	
Zr^{o}−Zr^{o}		Fe−Fe (2×)	3.626(1)
Zr1−Zr1 (2×)	3.626(1)		
		Te−Zr^{i}	
Zr^{o}−Zr^{i,N}		Te1−Zr2 (3×)	2.997(1)
Zr1−Zr2 (2×)	3.284(2)		
		Te−Zr^{o}	
Zr^{o}−Zr^{o,N}		Te1−Zr1 (6×)	2.975(1)
Zr1−Zr1 (4×)	4.085(4)		
		Te1−Te1 (2×)	3.626(1)

[a] Zr^{i}, Zr atom of inner trigonal prism; Zr^{o}, Zr atom capping the trigonal prism; Zr^{i,N}, inner Zr atom of the neighboring trigonal prism; and Zr^{o,N}, capping Zr atom of the neighboring trigonal prism.

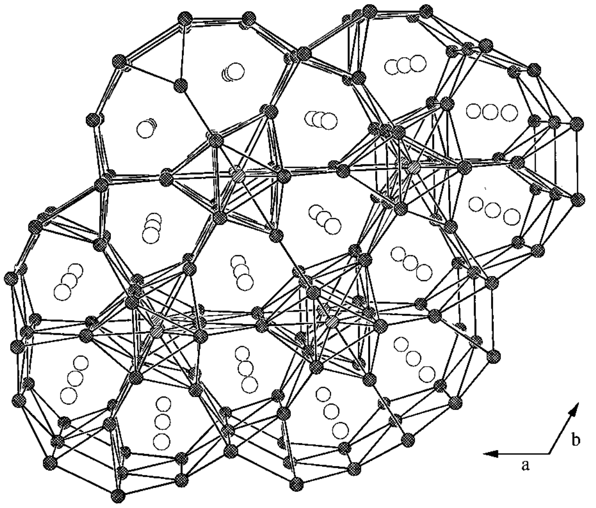

Figure 1. Approximate (001) projection of Zr_6FeTe_2 structures. The zirconium, iron, and tellurium atoms are shown as cross-hatched, hatched, and open circles, respectively. Bonds shown indicate the Zr−Zr and Zr−Fe contacts.

type (also called the K_2UF_6 type).[38] Other known zirconium intermetallics with this structure type are three aluminum-containing compounds (Zr_6MAl_2: M = Fe, Co, Ni),[34] one tin-containing compound (Zr_6FeSn_2), and several nonstoichiometric antimony phases $Zr_6M_{1-x}Sb_{2+x}$ (M = Fe, Co, Ni, Ru).[39] The Zr_6FeTe_2 structure is projected in perspective along the *c* axis in Figure 1; important bond distances are listed in Table 4. Chains of condensed Fe-centered zirconium tetrakaidecahedra (**1**) that form the basis of this structure are viewed down their 3-fold axes in this projection. The condensation of Zr_9Fe polyhedra is achieved by sharing of triangular Zr_3 faces. For the purposes of discussion we will adopt a notation wherein the "inner" Zr atoms of the trigonal prism that immediately surrounds each Fe center are labeled as Zr^{i} and the "outer" Zr atoms that cap the square faces of that prism are labeled as Zr^{o}. The formula for the Zr_6Fe chains depicted in **1** can then be written as ${}^{1}_{\infty}[Zr^{i}_{6/2}Zr^{o}_{3}Fe]$. The Zr−Zr-bonding network is completed by cross-linking Zr^{i} atoms of each chain with Zr^{o} atoms of neighboring chains to form the hexagonal "packing" of chains evident in Figure 1. This pleasing structural arrangement creates a slightly twisted tetrakaidecahedron of zirconium in which Te atoms reside. Thus, the zirconium cages that encapsulate iron and tellurium in this compound are quite similar in shape, though the cage surrounding tellurium is larger and less symmetrical (Fe, D_{3h}; Te, C_{3h}). The distances from Te atom to the capping zirconium atoms are 2.975(1) Å, and to the six Zr atoms of the prism they are 2.997(1) Å. The Zr−Zr bond distances of the triangular face in the trigonal prism are 4.085(4) Å. The shortest Te−Te contact is 3.626(1) Å, corresponding to the *c* axis stacking distance.

Regular (3-fold symmetric) zirconium tetrakaidecahedra are observed for compounds adopting hexagonal structure types, Zr_6MTe_2 (M = Mn, Fe, Co, Ni, Ru, Pt) and $Ta_9M_2S_6$ (M = Fe, Co, Ni)[21,22] compounds. The Fe-centered tetrakaidecahedra found in Nb_6FeS_2,[25] $Ta_9Fe_2S_6$,[22] and Hf_8FeTe_6[27] are much less symmetrical than the tetrakaidecahedron in Zr_6FeTe_2; a comparison is presented in **2**. The M_6 trigonal prisms are shaped such that equilateral triangular faces are observed in both Zr_6FeTe_2 and $Ta_9Fe_2S_6$ (d_{M-M} = 3 × 3.260 Å and 3 × 3.050 Å, respectively); these faces are isosceles triangles in Hf_8FeTe_6. The triangular faces in Nb_6FeS_2 are even less regular. Moreover, the (Zr, Hf)$_3$ triangles are more widely separated than those in the Zr_6FeTe_2 (3.626 Å) and the Hf_8FeTe_6 (3.731 Å) and are much longer than those of Nb_6FeS_2 and $Ta_9Fe_2S_6$ compounds. This separation generally corresponds to the shortest crystallographic axes for the compounds and is determined by the steric demands of the chalcogen atoms. As shown in Table 1, there is an expected expansion of both the *a* and *c* axis lengths on replacing Fe by Ru and Ni by Pt. While the Mn-centered compound has a larger cell volume, those of Fe, Co, and Ni are about equal. There is, however, a decrease of the *a* axis length and elongation of the *c* axis length on moving from Fe through Ni that may be associated with an increase of electron concentration.

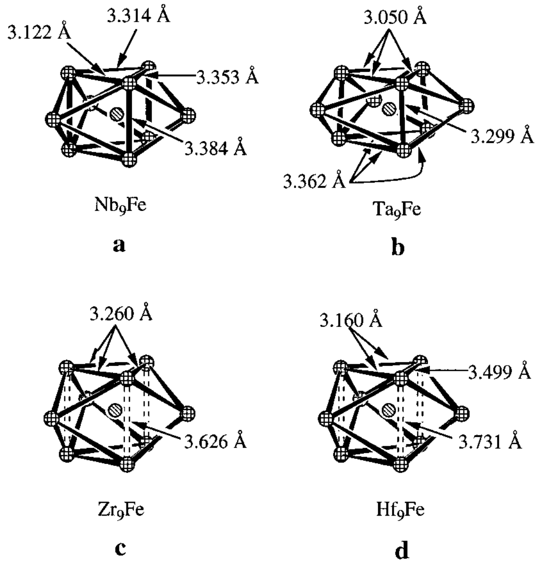

2

As we have noted, the tellurides discussed herein are isostructural with Zr_6MAl_2 (M = Fe, Co, Ni),[34] Zr_6FeSn_2, and $Zr_6M_{1-x}Sb_{2+x}$ (M = Fe, Co, Ni, Ru).[39] The observation of complete substitution of Al by both Sn and Te atoms and partial substitution by Sb demonstrates the flexibility of the structure. This flexibility is even more apparent when one examines relationships to binary compounds; when both Co and Al atoms are replaced by P and Zr atoms are replaced by Fe, the parent binary Fe_2P [≡ $Fe_6(P)P_2$] structure type emerges.[40] In this parent structure type then, all the tetrakaidecahedra are filled

---

(38) Villars, P.; Calvert, L. D. *Pearson's Handbook of Crystallographic Data for Intermetallic Phases*, 3rd ed.; American Society for Metals: Materials Park, OH, 1985; Vol. 1.

(39) Kwon, Y. U.; Sevov, S. C.; Corbett, J. D. *Chem. Mater.* **1990**, *2*, 550.

(40) Rundqvist, S. *Acta Chem. Scand.* **1959**, *13*, 425.

with the same "interstitials" (phosphorus in this case). Hundreds of compounds adopt the Fe_2P-type structure, most of which are ternary alloys in which segregation between sites like that seen for Zr_6MAl_2-type compounds has not been reported.[38] (See, however, a study of the site preferences in the Fe_2P-type $Hf_{1+x}Mo_{1-x}P$.[41]) Since both Fe and P sites in the Fe_2P structure can be filled by various atoms including rare earth elements, transition metals, and post-transition metals, the extent to which the structural stability is governed by the "size" and/or "electronic" effects is not clear, and further investigation of this problem is warranted.

$Zr_6(Fe_{0.6}Se_{0.4})Se_2$ and $Zr_6(Fe_{0.57}S_{0.43})S_2$. The discovery of Zr_6MTe_2 tellurides led us to seek sulfur and selenium analogs. Arc-melting reactions allowed us to quickly assess the feasibility of their synthesis, and the presence of a previously unidentified phase as the sole product in the powder diffraction patterns of the products indicated the existence of these new compounds. Instead of being isostructural with Zr_6FeTe_2, these compounds were found to adopt the Ta_2P-type structure,[42] and as such they are substitutional variants of the binaries Zr_2Q [$\equiv Zr_6(Q)Q_2$; Q = S, Se].[43–45] Interestingly, these new $Zr_6(Fe_{1-x}Q_x)Q_2$ compounds exhibit the same structure type and nonstoichiometric behavior as $Nb_6M_{1-x}S_{2+x}$ (M = Fe, Co, Ni; $0 < x < 0.4$) systems,[25,26] even though the binary parent compound "Nb_2S" ($x = 0$) is unknown.

Solid solution studies of $Zr_6(Fe_xSe_{1-x})Se_2$ ($x = 0.25$, 0.5, 0.75, 1.0) were carried out by reacting powders at 1000 °C for 2 weeks followed by arc-melting reaction of the products thereby obtained. In all cases, products from powder reactions contained the desired phase and Zr_3Se_2. When $x \geq 0.5$ the product of arc-melting reactions showed a single identifiable $Zr_6(Fe_xSe_{1-x})Se_2$ phase in the powder diffraction pattern. The cell parameters increased with increasing Fe content, indicating the possibility of obtaining the stoichiometric Zr_6FeSe_2 composition. However, we have not yet carefully delimited the range of possible compositions for this system. Phase segregation into the desired phase and Zr_3Se_2 was observed at lower Fe content ($x = 0.25$) before and after the arc-melting reaction. Like the Zr_6MTe_2 system, attempts to incorporate late transition metals for both sulfides and selenides were successful. The powder diffraction pattern of each product showed a single identifiable phase which exhibited significantly larger cell constants than those of corresponding binary ZrQ_2 (Q = S, Se). (See Supporting Information.) All of these systems are likely to exhibit substitutional variability as we have discussed above; this is currently under investigation.

A projection of the $Zr_6Fe_{0.6}Se_{2.4}$ structure down the *c* axis is shown in Figure 2, and the important bond distances of both $Zr_6Fe_{0.6}Se_{2.4}$ and $Zr_6Fe_{0.57}S_{2.43}$ are listed in Table 5. In these compounds, $^1_\infty[Zr^i_{6/2}Zr^o_3Fe(Q)]$ chains (**1**) are once again the basic structural motif. In this structure, however, chains cross-link in a less symmetrical way to form an orthorhombic structure (Figure 2) that provides smaller cavities than those that are needed for Zr_6FeTe_2 since smaller chalcogenides (Q = S, Se) are to be accommodated. Some of the edges of the $^1_\infty[Zr^i_{6/2}Zr^o_3Fe(Q)]$ chains are joined to form zigzag layers that propagate in the *ac* planes. This edge interconnection not only produces two zigzag ribbons of $Zr^i{-}Zr^o$ bonds between neighboring chains (2 × 3.173(2) Å and 2 × 3.305(2) Å (Se), 2 × 3.145(2) Å and 2 × 3.246(2) Å (S)) but also $Zr^i{-}Zr^i$ (2 × 3.325(2) Å (Se), 2 × 3.293(3) Å (S)) and $Zr^o{-}Zr^o$ (2 × 3.360(4) Å (Se), 2 × 3.319(2) Å (S)) bonds between adjacent chains—see Figure 3. The full three-dimensional metal–metal-bonding net is completed by forming additional $Zr^o{-}Zr^o$ and $Zr^i{-}Zr^o$ bonds that cross-link the layers. Two chalcogen atom sites (Q1 and Q2) between the layers are thus generated: Q1 is surrounded by a distorted monocapped trigonal prism of zirconium atoms with Zr–Q bond distances that range between 2.730(2) and 2.817(3) Å for selenide and between 2.636(4) and 2.757(4) Å for sulfide. A distorted bicapped trigonal prism of zirconium atoms envelop Q2: Zr–Q bond distances fall in the range from 2.738(2) to 2.989(3) Å for selenide and from 2.643(3) to 2.872(4) Å for sulfide. The shortest Q–Q contacts are between 3.581(1) Å and 3.497(1) Å for the selenide and sulfide, respectively.

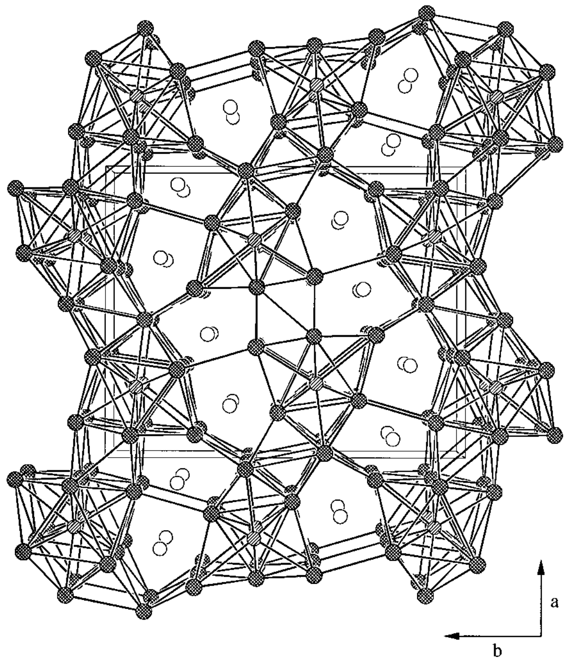

Figure 2. (001) projection of the $Zr_6Fe_{1-x}Q_{2+x}$ (Q = S, Se) structures. Zirconium, iron, and chalcogen atoms are shown as cross-hatched, hatched, and open circles, respectively. Bonds shown indicate the Zr–Zr and Zr–Fe contacts.

Unlike the regular Zr tetrakaidecahedra in Zr_6FeTe_2, those in both $Zr_6Fe_{0.6}Se_{2.4}$ and $Zr_6Fe_{0.57}S_{2.43}$ are appreciably distorted. The Q- and Fe(Q)-centered tetrakaidecahedra in the Zr_2Q, Nb_6FeS_2, and $Zr_6Fe_{1-x}Q_{2+x}$ compounds show some similarities to those of the binary alloy, Zr_3Fe.[46,47] A comparison of selected bond distances can be made by use of the data listed in Table 6. The prisms commonly possess one small and two large rectangular faces that are respectively associated with one long and two short Zr^o–Fe contacts. Both the longest M–Fe (M = Zr, Nb) and Zr–Q (Q = S, Se) bond distances result from the steric demands of the rectangular face with short M–M bonds. Comparison between Zr_2S and $Zr_6Fe_{0.57}S_{2.43}$ and among the $Nb_6M_{1-x}S_{2+x}$ compounds shows that both M–M and M–Fe(S) bond distances in the tricapped trigonal prisms decrease slightly upon replacement of S by Fe.

Electronic Band Structures of Zr_6FeTe_2 and Zr_6FeSe_2. The electronic band structures of both Zr_6FeTe_2 and idealized (stoichiometric) Zr_6FeSe_2 were calculated using the extended Hückel method.[48] The parameters are given in Table 7.[49] Our discussion here will be brief, since these results parallel those recently published for Hf_8MTe_6 and Hf_5FeTe_3.[27,28]

---

(41) Miller, G. J.; Cheng, J. *Inorg. Chem.* **1995**, *34*, 2962.
(42) Nylund, A. *Acta Chem. Scand.* **1966**, *20*, 2393.
(43) Conard, B. R.; Franzen, H. F. *High Temp. Sci.* **1971**, *3*, 49.
(44) Yao, X.; Franzen, H. F. *J. Less-Common Met.* **1988**, *142*, L27.
(45) Franzen, H. F.; Norrby, L. J. *Acta Crystallogr.* **1968**, *B24*, 601.
(46) Buschow, K. H. J. *J. Less-commom Met.* **1981**, *79*, 243.
(47) Boller, H. *Monatsh. Chem.* **1973**, *104*, 545.
(48) Hoffmann, R. *J. Chem. Phys.* **1963**, *39*, 1397.
(49) Clementi, E.; Roetti, C. *At. Data Nucl. Data Tables* **1974**, *14*, 177.

Table 5. Important Interatomic Distances (Å) for $Zr_6Fe_{0.6}Se_{2.4}$ and $Zr_6Fe_{0.57}S_{2.43}$[a]

	S	Se		S	Se		S	Se
Zr^i-Zr^i			$Zr^i-Zr^{o,N}$			(Fe,Q)$-Zr^o$		
Zr2−Zr2 (2×)	3.497(1)	3.581(1)	Zr2−Zr1 (1×)	3.497(1)	3.591(2)	Fe−Zr1 (1×)	3.079(4)	3.055(3)
Zr2−Zr5 (1×)	3.527(2)	3.496(3)	Zr5−Zr3 (2×)	3.246(2)	3.305(2)	Fe−Zr3 (1×)	2.891(3)	2.942(3)
Zr2−Zr6 (1×)	3.338(2)	3.370(2)	Zr6−Zr1 (2×)	3.145(2)	3.173(2)	Fe−Zr4 (1×)	3.192(4)	3.222(3)
Zr5−Zr2 (1×)	3.527(2)	3.496(3)						
Zr5−Zr5 (2×)	3.497(1)	3.581(1)	$Zr^i-Zr^{i,N}$			Q$-Zr^i$ (Zr^o)		
Zr5−Zr6 (1×)	3.452(2)	3.526(3)	Zr6−Zr6 (1×)	3.293(3)	3.325(3)	Q1−Zr1 (1×)	2.636(4)	2.730(2)
Zr6−Zr2 (1×)	3.338(2)	3.370(2)				Q1−Zr2 (1×)	2.645(4)	2.746(3)
Zr6−Zr5 (1×)	3.452(2)	3.526(3)	$Zr^o-Zr^{o,N}$			Q1−Zr3 (1×)	2.757(4)	2.817(3)
Zr6−Zr6 (2×)	3.497(1)	3.581(1)	Zr1−Zr4 (1×)	3.602(2)	3.690(2)	Q1−Zr4 (2×)	2.646(3)	2.738(2)
			Zr3−Zr3 (1×)	3.319(2)	3.360(4)	Q1−Zr5 (2×)	2.684(3)	2.784(2)
Zr^i-Zr^o			Zr3−Zr3 (2×)	3.497(1)	3.581(1)	Q2−Zr1 (2×)	2.704(3)	2.792(2)
Zr2−Zr3 (2×)	3.155(2)	3.206(2)	Zr3−Zr4 (4×)	3.166(2)	3.300(2)	Q2−Zr2 (2×)	2.696(3)	2.781(2)
Zr2−Zr4 (2×)	3.332(2)	3.368(2)	Zr4−Zr4 (1×)	3.688(3)	3.866(2)	Q2−Zr3 (1×)	2.872(4)	2.989(3)
Zr5−Zr1 (2×)	3.345(2)	3.443(2)				Q2−Zr4 (2×)	2.643(3)	2.738(2)
Zr5−Zr3 (2×)	3.146(2)	3.156(2)	(Fe,Q)$-Zr^i$			Q2−Zr6 (1×)	2.821(4)	2.885(3)
Zr6−Zr1 (2×)	3.108(2)	3.098(2)	Fe−Zr2 (2×)	2.639(3)	2.671(2)			
Zr6−Zr4 (2×)	3.153(2)	3.181(2)	Fe−Zr5 (2×)	2.681(3)	2.700(2)	Q−Q		
			Fe−Zr6 (2×)	2.618(3)	2.682(2)	Q1−Q1 (1×)	3.497 (1)	3.581 (1)
						Q1−Q2 (2×)	3.668 (2)	3.685 (2)

[a] Zr^i, Zr atom of inner trigonal prism; Zr^o, Zr atom capping the trigonal prism; $Zr^{i,N}$, inner Zr atom of the neighboring trigonal prism; and $Zr^{o,N}$, capping Zr atom of the neighboring trigonal prism.

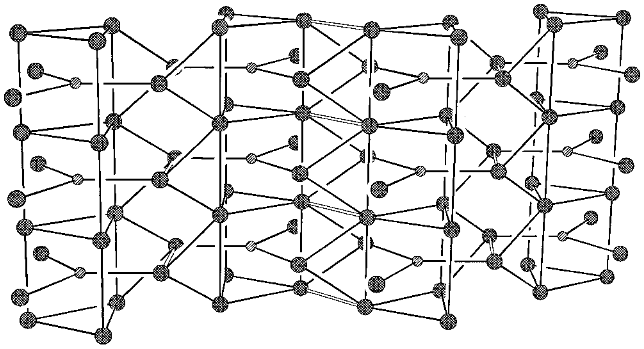

Figure 3. Edge interconnetions for $^1_\infty[Zr_6Fe]$ chains are projected in perspective on the *ac* plane. Zr atoms are shown as cross-hatched circles and Fe atoms as hatched circles. Some Zr−Zr bonds are omitted for clarity.

Table 6. Bond Distance (Å) Comparison of the Tricapped Trigonal Prisms[a] in Binary and Ternary Zirconium Compounds

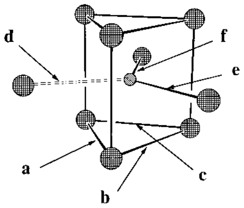

	M−M[b], Å			M−Fe/Q, Å		
compound	*a*	*b*	*c*	*d*	*e*	*f*
Zr_3Fe	3.313	3.608	3.608	3.493	3.056	3.056
Zr_2S	3.242	3.547	3.556	3.326	2.903	2.774
$Zr_6Fe_{0.57}S_{2.43}$	3.338	3.527	3.452	3.192	2.891	3.079
Nb_6FeS_2	3.119	3.311	3.350	3.019	2.711	2.764
Zr_2Se	3.347	3.639	3.732	3.364	2.858	2.941
$Zr_6Fe_{0.6}Se_{2.4}$	3.370	3.495	3.526	3.222	2.942	3.055

[a] Fe, S, Se, Fe/S, and Fe/Se atoms are shown as hatched circles; Zr atoms are shown as black circles. [b] Columns *a*, *b*, and *c* denote M−M bond distances; columns *d*, *e*, and *f* denote distances of M−Fe/Q bonds.

Table 7. Parameters for EH Calculations for Zr_6FeTe_2 and Zr_6FeSe_2

	orbital	H_{ii}, eV	ζ_1[b]	ζ_2[b]	C_1[a]	C_2[a]
Zr	4d	−6.81	3.84	1.505	0.6213	0.5798
	5s	−7.22	1.82			
	5p	−3.77	1.78			
Fe	3d	−7.93	5.55	1.800	0.5411	0.6734
	4s	−6.84	1.90			
	4p	−3.19	1.90			
Te	5s	−21.20	2.51			
	5p	−12.00	2.16			
Se	4s	−21.50	2.43			
	4p	−13.00	2.07			

[a] Coefficients used in double-ζ expansion. [b] Slater-type orbital exponents.

The total density of states (DOS) diagrams of both compounds (Figures 4 and 5) show that the materials should be metallic, as would be intuitively expected for structures containing a metal−metal-bonded framework. Inspection of the projected DOS diagrams in Figure 4, part b, and Figure 5, part b, show that the energy levels below −10.5 eV are primarily Te- and Se-based manifolds. The projected DOS diagrams in Figure 4, part c, and Figure 5, part c, show that levels with Fe character span the range between −10.5 and −4.0 eV for both compounds, while the projections in panel d of both figures show that levels at higher energy have mainly Zr d and s character. The projected DOS diagrams show significant mixing of zirconium character in the Te- and Se-based manifolds, respectively, indicating significant Zr−Q covalency.

The spatial segregation of the Fe and chalcogen atoms within the Zr_6FeTe_2 and Zr_6FeSe_2 structures, respectively, are also manifest in both electronic structures. The Fe contributions to the DOS of both compounds are all in the range between −10.5 and −4.0 eV. Although the energy separation of Fe 3d, Se 4p, and Te 5p orbitals is small, the levels with Fe character are virtually excluded from both Te- and Se-based manifolds. The projected DOS diagrams for both the telluride and selenide compounds show a clear delineation of Zr−Fe- and Zr−Q-bonding levels. Of course, there are no Fe−Te and Fe−Se bonds in either compound, and the electronic structures naturally reflect their absence.

Crystal orbital overlap populations (COOPs) were also calculated for the metal−metal-bonded framework in the Zr_6FeTe_2 and Zr_6FeSe_2 structures. The COOP curves of Zr−Fe and Zr−Zr interactions and of Zr−Fe and Zr−Zr interactions for Zr_6FeTe_2 and Zr_6FeSe_2 are shown in Figure 6. In both compounds, crystal orbitals with significant Zr−Zr-bonding character extend above the Fermi level, but Zr−Fe-bonding character appears to be optimal for the electron concentrations appropriate for these compounds. The optimization of early−

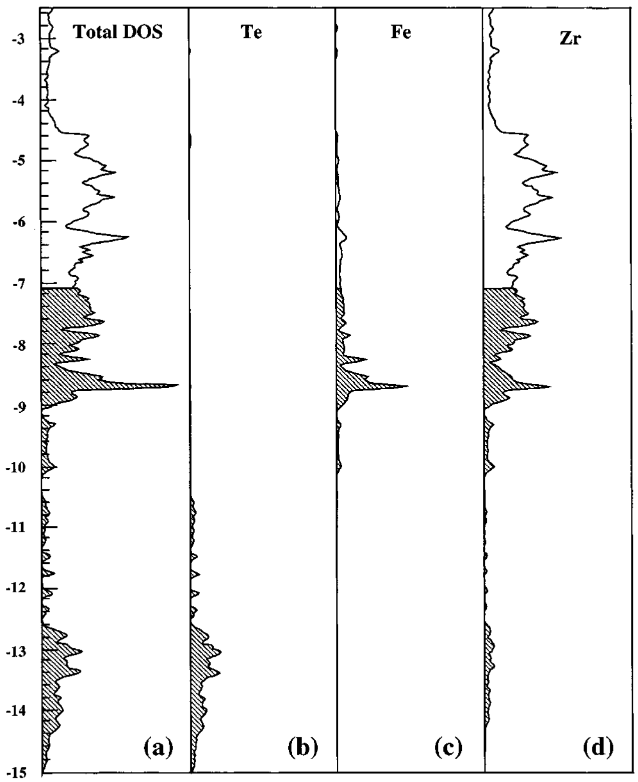

Figure 4. Total density of states (DOS) diagram for Zr_6FeTe_2 (a) and projected DOS of Te (b), Fe (c), and Zr (d) are shown. Filled levels are shaded.

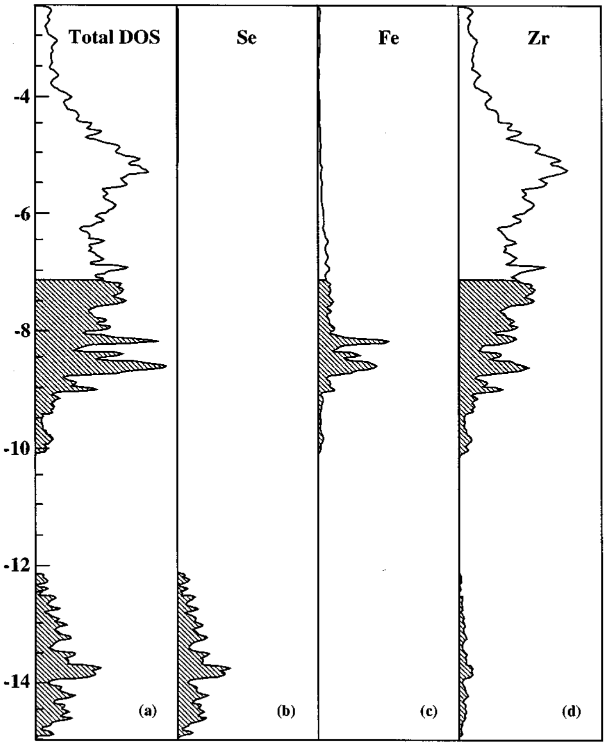

Figure 5. Total density of states (DOS) diagram for $Zr_6Fe_{0.6}Se_{2.4}$ (a) and projected DOS of Se (b), Fe (c), and Zr (d) are shown. Filled levels are shaded.

late transition intermetallic bonding that we have noted on several previous occasions is again implicated as a key feature stabilizing these new compounds.

It is important to note that the existence of $Nb_6M_{1-x}S_{2+x}$ compounds that are isostructural, but not isoelectronic, with $Zr_6Fe_{1-x}Se_{2+x}$ raises questions about the bonding analysis given above. Comparison of Zr–Zr distances in Zr_2S or $Zr_6Fe_{0.57}S_{2.43}$ with Nb–Nb distances in the $Nb_6M_{1-x}S_{2+x}$ compounds leads to the conclusion that Nb–Nb bond orders are significantly higher, even after allowing for a change in atomic radius (metallic single bond distances, d_1(Nb–Nb) = 2.71 Å, d_1(Zr–Zr) = 2.92 Å). If we uncritically accept the band structure for Zr_6FeSe_2 as appropriate for a niobium analog, the higher electron concentration appropriate for Nb_6FeSe_2 (and correspondingly higher Fermi energy) would lead to the occupation of crystal orbitals with Nb–Fe-antibonding character. If we abandon the rigid-band picture, in which one assumes that crystal orbital energies and character are approximately independent of whether such orbitals are occupied, then this seeming contradiction may be resolved. A more thorough analysis of these problems will be deferred to a separate investigation.

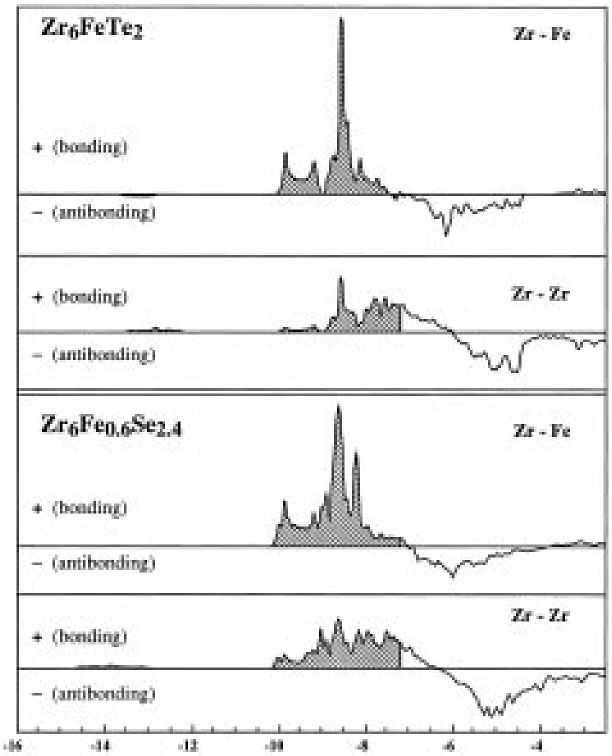

Figure 6. Averaged crystal orbital overlap population (COOP) curves for Zr–Fe and Zr–Zr contacts less than 3.2 and 3.7 Å, respectively, in both the Zr_6FeTe_2 and $Zr_6Fe_{0.6}Se_{2.4}$ are shown. Levels above horizontal axes are bonding (+) while below are antibonding (−). Filled levels are shaded. Note optimization of the Zr–Fe interactions in Zr_6FeTe_2.

Structural Relationships. As we have seen, sulfide, selenide, and telluride compounds of the Zr_6MQ_2 composition have different structures. The telluride adopts the ternary alloy Zr_6CoAl_2-type structure (an ordered Fe_2P variant) and both the sulfide and selenide adopt a structure derived from the Ta_2P type. The most obvious rationalization for this difference is the differential in atomic size of the chalcogens. The larger Te atoms naturally adopt a higher coordination number (nine-coordinate in this compound), and the wide open channels in the Zr_6FeTe_2 structure are the result. In $Zr_6Fe_{1-x}Q_{2+x}$, the structure rearranges to offer smaller seven- and eight-coordinate chalcogen sites, while retaining $^1_\infty[Zr^i_{6/2}Zr^o_3Fe(Q)]$ chains. Correlated with the closer Fe–Q size match for Q = S, Se is the fact that Zr_6FeTe_2 is stoichiometric while the $Zr_6Fe_{1-x}Q_{2+x}$ phases apparently exhibit appreciable phase width.

The structural relationship between the recently discovered Hf_8FeTe_6[27] and Zr_6FeTe_2 is made apparent by reference to Figure 7, where we show projections of the Hf_8FeTe_6 and Zr_6FeTe_2 structures onto *ac* and *ab* planes, respectively. If the Hf_8FeTe_6 structure is partitioned into two-dimensional slabs as indicated in Figure 7, the compound can be recognized as an

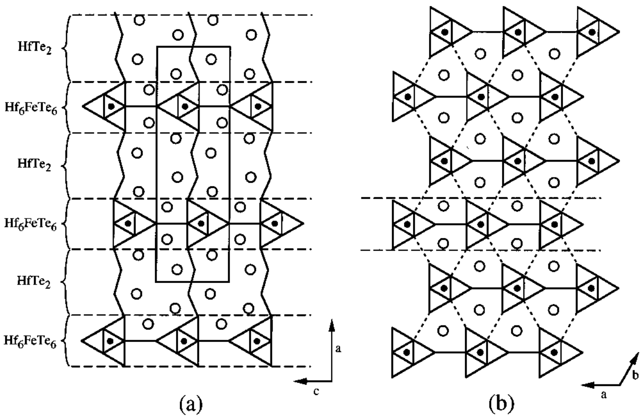

Figure 7. Schematic *b*- and *c*-axis projections of Hf_8FeTe_6 and Zr_6FeTe_2 are shown in (a) and (b), respectively. Fe atoms are shown as filled circles within the tricapped trigonal prisms and Te atoms as open circles. Only Hf−Hf and Zr−Zr bonds within and between chains are shown.

intergrowth of the simple binary $HfTe_2$ and Hf_6FeTe_2 [$Hf_8FeTe_6 \equiv (Hf_6FeTe_2)(HfTe_2)_2$]. Note that the "proper" assembly of the Hf_8FeTe_6 structure requires that every second $^{2}_{\infty}[Hf_6FeTe_2]$ slab must be "flipped" by 180° before it is stacked upon the previous $HfTe_2$ spacer material. It can be seen that the two-dimensional $^{2}_{\infty}[Hf_6FeTe_2]$ slabs imbedded in the Hf_8FeTe_6 structure exhibit precisely the same linkages between $^{1}_{\infty}[Hf^{i}_{6/2}Hf^{o}_{3}Fe]$ chains that we have discussed for analogous zirconium chains in Zr_6FeTe_2. In Zr_6FeTe_2 these chains are fully cross-linked in three dimensions, while in Hf_8FeTe_6 the metal−metal bonding present within the $^{2}_{\infty}[Hf_6FeTe_2]$ slabs is interrupted by the intergrowth of the more oxidized $HfTe_2$. If we assume that the metal−metal bonding between hafnium centers within the $HfTe_2$ region of Hf_8MTe_2 is negligible, then the electron concentration within the remainder of the Hf−M framework is identical to the electron concentration in Zr_6MTe_2 compounds.

The structure of ternary $Zr_6Fe_{1-x}Q_{2+x}$ (Q = S, Se) compounds shown in Figure 2 can be viewed as composed of zigzag ribbons running parallel along the *a* axis. These zigzag ribbons are then cross-linked by additional $Zr^{o}-Zr^{o}$ and $Zr^{i}-Zr^{o}$ bonds along the *b* axis to complete the three-dimensional structure. Similar zigzag ribbons are also observed in the structure of the binary alloy Zr_3Fe.[46,47] The structure of Zr_3Fe is shown in perspective on the *bc* plane in Figure 8. The COOP curves show the optimization of Zr−Fe-bonding characters, indicating the stabilization of the structure conferred by strong early−late transition metal bonding.[50] As the structure can be conceptually torn apart along the c axis shown in Figure 8, part b, we recognize zigzag layers propagating in the *ab* plane that are closely similar to those we have described for $Zr_6Fe_{1-x}Q_{2+x}$ above. From this point of view, the Zr_3Fe structure can be described as a full condensation of these zigzag layers along the *b* axis, while the "extraction" of the zigzag layers is achieved by oxidation of Zr_3Fe with chalcogen (S and Se).

Concluding Remarks

The newly discovered metal-rich Zr_6MTe_2 (M = Mn, Fe, Co, Ni, Ru, Pt), $Zr_6Fe_{0.6}Se_{2.4}$, and $Zr_6Fe_{0.57}S_{2.43}$ belong to a growing family of compounds whose structures are characterized chains of condensed M-centered tetrakaidecahedra. The encapsulation of all late transition metals in ternary zirconium chalcogenides demonstrates the flexibility of the tetrakaidecahedral building block. The Zr_6MTe_2 compounds are isotypic with Zr_6MAl_2 intermetallics, but also serve as a missing link between such conventional intermetallics such as Zr_3Fe and the more structurally open Hf_8MTe_6. These structural connections also lead us to wonder whether series of compounds with the general formula $Hf_{6+n}MTe_{2+2n}$ [$\equiv (Hf_6FeTe_2)(HfTe_2)_n$] might be synthesized. This link helps to clarify how binary intermetallics (like Zr_3Fe) that have substantially negative heats of formation are still thermodynamically unstable with respect to the formation of the ternaries such as those reported here. The early−late transition metal bonding is entirely preserved on the formation of the ternaries and the nominal oxidation of Zr_3Fe by chalcogens occurs at the expense of weaker Zr−Zr bonds.

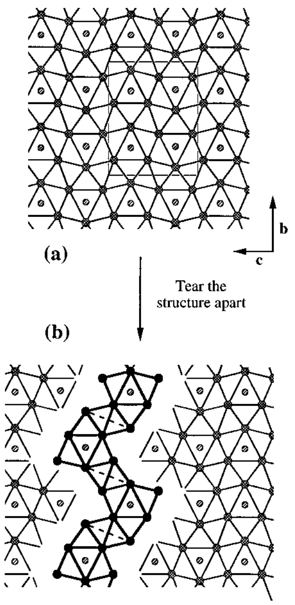

Figure 8. The projection of the Zr_3Fe structure along the *a* axis is shown in (a). Zr atoms are shown as cross-hatched circles and Fe atoms as hatched circles. The structure can be torn apart to reveal the imbedded zigzag layer (b) which, with minor rearrangement shown with dashed lines, forms the basis of the $Zr_6Fe_{1-x}Q_{2+x}$ (Q = S, Se) structure (compare Figure 2). Zr−Fe linkages are omitted for clarity.

Acknowledgment. This research was generously supported by the National Science Foundation through Grant DMR-9215890 and by the Robert A. Welch Foundation through Grant A-1132. The R3m/v and P4 single-crystal X-ray diffractometer and crystallographic computing system were purchased from funds provided by the National Science Foundation (Grant CHE-8513273). We thank Dr. Joseph Reibenspies for helping in the collection of data on the P4 diffractometer. We also thank Dr. Renald Guillemette for his assistance with the microprobe analyses.

Supporting Information Available: Three X-ray crystallographic files, in CIF format, are available. Access information is given on any current masthead page.

IC960610T

---

(50) Hughbanks, T.; Rosenthal, G.; Corbett, J. D. *J. Am. Chem. Soc.* **1988**, *110*, 1511.